



Research article

Strengthening and toughening bulk Ni₂CoFeV_{0.5} medium-entropy alloy via thermo-mechanical treatment



Lei Gu¹, Rui Hou¹, Yi Liu, Guang Chen*, Jihua Liu, Gong Zheng, Ruisheng Zhang, Yonghao Zhao*

National Key Laboratory of Advanced Casting Technologies, MIIT Key Laboratory of Advanced Metallic and Intermetallic Materials Technology, Engineering Research Center of Materials Behavior and Design, Ministry of Education, Nanjing University of Science and Technology, Nanjing 210094, China

ARTICLE INFO

Article history:

Received 25 October 2022

Revised 16 November 2022

Accepted 17 November 2022

Available online 11 February 2023

Keywords:

Medium-entropy alloys

Microstructures

Strength and ductility

Heterogeneous lamella structure

Cold-rolling

Annealing

ABSTRACT

Single-phase face-centered cubic (fcc) medium- and high-entropy alloys (MEAs/HEAs) have high ductility but low yield strength. In this work, the microstructures of single-phase fcc Ni₂CoFeV_{0.5} MEAs were tailored by cold-rolling and subsequent annealing and typical heterogeneous lamella (HL) structures composed of recrystallized micro-grain lamellae (with an averaged grain size of ~4 μm) and non-recrystallized nano-/ultrafine-grain lamellae were obtained. Tensile tests revealed that most HL samples exhibited excellent strength and ductility synergy. The HL sample with ~23 vol% recrystallized grains annealed at 590 °C for 1 h had a high yield strength of 1120 MPa and a good fracture elongation of 12.3%, which increased by 5% and 46%, respectively compared with those of as-rolled sample. Annealing-induced yield strength increase is attributed to high-density annealing twin boundaries (TBs) in the recrystallized grains, the annihilation of mobile dislocations inside the non-recrystallized grains, and extra hetero-deformation-induced strengthening produced by the HL structure. Hall-Petch relationship of Ni₂CoFeV_{0.5} MEA can be reasonably described by counting both TBs and grain boundaries, with lattice friction stress of 87.3 MPa and coefficient of 722.8 MPa μm^{1/2}. Our work provides optional and controllable solutions for preparing MEAs/HEAs with excellent mechanical properties by low-cost and high-efficiency thermo-mechanical treatments.

© 2023 Published by Elsevier Ltd on behalf of The editorial office of Journal of Materials Science & Technology.

1. Introduction

The development of advanced structural materials has been plagued by a well-known strength-ductility trade-off. In most cases, the tensile yield strength (YS) enhances at the expense of ductility, and vice versa. Among the four traditional strengthening theories, solid-solution strengthening, i.e. microalloying, is the best method to improve strength while maintaining ductility as much as possible. Based on this, a class of super solid solution alloys, that is medium- and high-entropy alloys (MEAs/HEAs) proposed in 2004, are reported to exhibit an outstanding combination of strength and ductility [1–5]. Normally, equiatomic or near-equiatomic principal elements of MEAs are greater than three, and counterparts of HEAs are greater than five, and their configurational entropies are larger than 1R and 1.5R ($R = 8.314 \text{ J mol}^{-1} \text{ K}^{-1}$), respectively [6]. In the last twenty years, multisystem MEAs/HEAs

have been developed and exhibit outstanding performances, such as high strength [3,7,8], high hardness [9–11], excellent irradiation resistance [12,13], high plasticity [14], and so on. Typically, multi-component high-entropy Cantor alloy (CrMnFeCoNi) and its derivatives with single-phase face-centered cubic (fcc) structure have high strength, good ductility, and excellent fracture toughness at room and cryogenic temperatures [15–17].

A growing body of research suggests that increasing the lattice distortion by introducing different-sized atoms in single-phase fcc MEAs/HEAs can elevate simultaneously the strength and ductility, resulting from the enhanced resistance of dislocation slip by chemical short-range order [18,19]. For instance, the large-sized Al and Ti added into Ni₂CoCrFe alloy [20], the small-sized Si substituting Mn in Cantor alloy [21] and interstitial N-doped FeMnCoCr HEA [22] can effectively break the strength-ductility trade-off. Nevertheless, the improvement of strength only by solid-solution strengthening is limited. Actually, introducing the nano-precipitated phase in the ductile fcc MEAs/HEAs matrix can greatly increase the YS [23–27]. Precipitation strengthening plays an important role in strengthening HEAs because the

* Corresponding authors.

E-mail addresses: gchen@njust.edu.cn (G. Chen), yhzhao@njust.edu.cn (Y. Zhao).

¹ These authors contributed equally to this work.

second phase can easily form due to high mixing enthalpy. Creatively, Yang et al. [23] designed a nanoprecipitate-strengthened (FeCoNi)₈₆Al₇Ti₇ alloy with high-density L1₂-type multicomponent intermetallic nanoparticles. This dual-phase alloy exhibits superior ultimate tensile strength (UTS) of 1.5 GPa and high ductility of 50% at ambient temperature [23], drastically surpassing FeCoNi MEA matrix (UTS: ~510 MPa, ductility: ~32%) [24]. Likewise, a bi-functional L1₂ nanoprecipitate, which can strengthen the matrix and constrain martensitic transformation after quenching, was introduced into Fe-Ni-Al-Ti MEA and cause simultaneous enhancement of UTS and uniform elongation [25]. Although the ductile L1₂-phase can efficaciously achieve an excellent strength and ductility synergy, most precipitated phases in MEAs/HEAs, such as B2, σ , μ , Laves, and carbide, are hard to deform and even brittle, which destroy the ductility [26]. With the volume fraction of Laves phase increased, the YS of CoCrFeNi-(Nb, Mo) HEAs increased from 160 to 692 MPa but the total elongation sharply decreased from 65% to 7.5% [27]. The cleavage fracture of the hexagonal close-packed (hcp) Laves phase brought about poor ductility. Moreover, the size and geometry of the precipitates largely affect the strength-ductility trade-off. The large-sized precipitates are hard to overcome the strength-ductility trade-off [26]. In general, the ductility of fcc MEAs/HEAs is severely reduced by bringing in the precipitated phases. Besides, as an auxiliary deformation mechanism, mechanical twinning and phase transformation are able to improve the tensile strength dynamically in MEAs/HEAs with low stacking fault energy (SFE) [15,28,29], due to twinning-induced-plasticity (TWIP) and transformation-induced-plasticity effects. Li et al. [29] contrived a metastable Fe₅₀Mn₃₀Co₁₀Cr₁₀ HEA with UTS of ~860 MPa and excellent ductility of ~75% at the average grain size of ~4.5 μ m. Dynamic phase transformation from the fcc γ phase to the hcp ϵ phase and deformation-induced twinning in the hcp ϵ phase contributed to the enhanced strain hardening capacity in Fe₅₀Mn₃₀Co₁₀Cr₁₀ HEA. Regrettably, the YS of fully-recrystallized Fe₅₀Mn₃₀Co₁₀Cr₁₀ HEA was less than 350 MPa, limiting the structural engineering applications.

In addition to compositional design, tuning the microstructures can also balance the strength and ductility in both MEAs/HEAs and traditional alloys [30–34]. For single-phase fcc MEAs/HEAs, grain boundary (GB) strengthening and dislocation strengthening are the dominant methods to improve the YS. However, the total tensile elongation inevitably diminishes with the decreased grain size and the increased dislocation density. Recently, to obtain the optimal combination of strength and ductility, heterogeneous structures including gradient structure, bi-/multi-modal structure, heterogeneous lamella (HL) structure, harmonic structure, etc., were widely constructed in traditional alloys [35]. In a similar vein, a handful of studies have shown that the heterostructured MEAs/HEAs overcame the strength-ductility trade-off [36–38]. Pan et al. [36] introduced a heterogeneous gradient dislocation cell structure (GDS) in a fine-grained (FG) Al_{0.1}CoCrFeNi HEA and enhanced the strength without apparent loss of ductility. Both GDS HEAs had higher YSs of ~362 and ~539 MPa, about two to three times as strong as the FG sample (YS: ~185 MPa). Furthermore, the ductility of both GDS HEAs was ~65%, which is slightly reduced relative to the FG sample (~70%). Yin et al. [37] tried to construct an HL structure in Fe₃₅Ni₃₅Cr₂₅Mo₅ MEA, which consists of coarse-grained (CG) fcc matrix lamellae, and ultrafine-grained lamellae together with nanoprecipitates. This HL MEA had an excellent tensile property with the YS over 1.0 GPa and total elongation of ~13%. In addition to extra hetero-deformation induced (HDI) strengthening, precipitation strengthening also contributed to the high YS. SF-induced plasticity and TWIP played a key role in retaining good ductility of both the above-mentioned Al_{0.1}CoCrFeNi HEA and Fe₃₅Ni₃₅Cr₂₅Mo₅ MEA [36,37].

In this work, the microstructures of single-phase fcc Ni₂CoFeV_{0.5} MEAs were tailored by cold-rolling combined with subsequent annealing. Specifically, the HL structures were introduced into Ni₂CoFeV_{0.5} MEAs by long-time annealing at intermediate temperature, in order to obtain controllable properties with the optimal strength and ductility synergy. The microstructural evolutions of the cold-rolled and annealed samples were investigated by electron backscattered diffraction (EBSD) characterization in detail. Transmission electron microscopy (TEM) and high-resolution TEM focusing on the HL sample annealed at 600 °C for 3 h revealed that dislocation slip is the dominating deformation mechanism and high-density annealing twin boundaries (TBs) strengthen the recrystallized grains (RGs) by hindering dislocation slip. Furthermore, the cyclic load-unload-reload (LUR) tensile tests were performed to reveal the effect of HDI strengthening and hardening.

2. Experimental materials and procedures

2.1. Sample preparation

The bulk Ni₂CoFeV_{0.5} (atomic ratios) MEA ingot was prepared with commercial metals (Purity > 99.95%) by induction melting and was re-melted at least four times to ensure chemical homogeneity. The MEA ingot was cut into a plate and then was cold-rolled from 16 to 1.6 mm with a thickness reduction of ~90% at room temperature (designated as CR90 sample). Specimens cut from the cold-rolled sheet were annealed at temperatures ranging from 590 to 900 °C for 30 min to 3 h under an Ar atmosphere. The as-annealed samples with HL structures were labeled as HL-590 °C-1 h, HL-600 °C-3 h, HL-620 °C-30 min, and HL-620 °C-1 h samples, respectively, based on different annealing conditions.

2.2. Tensile testing

The tensile tests were performed using an LTM-20KN testing machine with a constant strain rate of 10⁻³ s⁻¹ at room temperature. Flat dog-bone-shaped tensile specimens with a gauge cross-section of 2.5 mm × 1.5 mm and a length of 10 mm were electro-discharge machined from the cold-rolled and as-annealed specimen sheets. The tensile specimen axis was parallel to the rolling direction. At least three tensile specimens were prepared for each sample to obtain repeatable experimental results. The cyclic LUR tensile tests were performed to measure the HDI stresses. During the LUR tensile tests, the specimens with HL structures were tensioned to an assigned strain of 1%, unloaded to 50 N, and then reloaded.

2.3. Microstructure characterizations

Microstructural evolutions and element distribution of the as-cast and cold-rolled Ni₂CoFeV_{0.5} MEA samples after partial and full recrystallization annealing were characterized by scanning electron microscopy (SEM) equipped with energy dispersive spectroscopy (EDS) and EBSD detectors. The EDS and EBSD specimens were mechanically polished first and then followed by electro-polishing using an electrolyte consisting of 90 vol.% acetic acid and 10 vol.% perchloric acid with a voltage of 35 V at room temperature. EBSD measurements were performed on an Oxford Instruments Aztec system and the scanning step size was chosen as 0.5 μ m for all samples. The commercial channel 5 software was used to analyze the EBSD data. The phase structures were characterized by Bruker-AXS D8 Advance X-ray diffraction (XRD) with the angle of 2 θ scanning from 30° to 90° and a scanning speed of 2° min⁻¹. The specimens for TEM observation were electro-polished in a twin jet

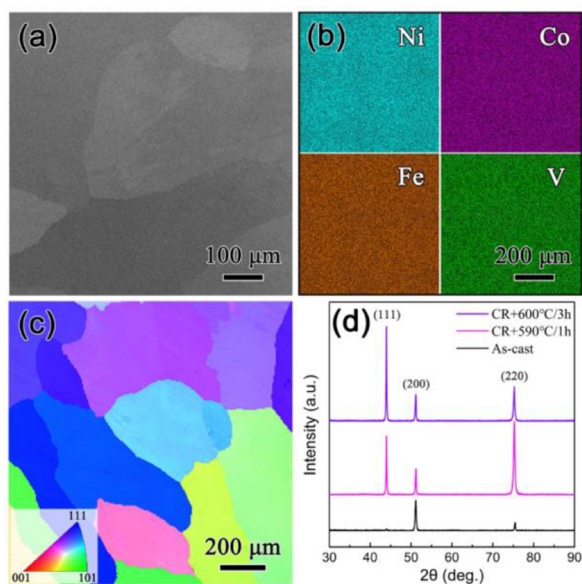


Fig. 1. (a) SEM image, (b) the corresponding EDS mappings, and (c) EBSD crystal orientation map of the as-cast $\text{Ni}_2\text{CoFeV}_{0.5}$ MEA. The inset in (c) is Inverse Pole Figure (IPF) color code. (d) XRD patterns of the as-cast and subsequently thermo-mechanical treated $\text{Ni}_2\text{CoFeV}_{0.5}$ MEAs.

Table 1

Chemical compositions of the as-cast $\text{Ni}_2\text{CoFeV}_{0.5}$ MEA (at.%).

Elements	Ni	Co	Fe	V
Concentration	43.7	22.5	22.6	11.2

electro-polishing system containing an electrolyte consisting of 10% perchloric acid, 20% glycerol, and 70% methanol at -20°C , and then observed by an FEI-Tecna G^2 20 S-TWIN microscope operating at 200 kV. High-resolution TEM observations were performed by a Titan G^2 60-300 microscope operating at 300 kV.

3. Results

3.1. Microstructural evolution during thermo-mechanical treatments

3.1.1. Initial microstructures

All the alloying elements (Ni, Co, Fe, V) in the as-cast $\text{Ni}_2\text{CoFeV}_{0.5}$ MEA are homogeneously distributed in the range of grain scale (Fig. 1(a, b)), indicating a single-phase solid solution without the secondary phase. The measured chemical composition from EDS data is shown in Table 1, which is generally consistent with the nominal composition. It consists of randomly oriented sub-millimeter-sized grains with an average grain size of $\sim 320\ \mu\text{m}$, as shown in Fig. 1(c). The as-cast $\text{Ni}_2\text{CoFeV}_{0.5}$ MEA is a single-phase fcc structure, further confirmed by the XRD result in Fig. 1(d).

3.1.2. Microstructures of cold-rolled sample

EBSD and TEM results of the CR90 $\text{Ni}_2\text{CoFeV}_{0.5}$ sample are shown in Fig. 2. The crystal orientation map with the color code (red, green, and blue indicate grains have $\langle 001 \rangle$, $\langle 110 \rangle$, and $\langle 111 \rangle$ directions parallel to transverse direction) shows that the initial sub-millimeter-sized grains were flattened and elongated along the rolling direction, and a large number of randomly oriented fine grains were produced by dynamic recrystallization during cold-rolling processing (Fig. 2(a)). Moreover, local severe deformation generated large lattice distortion, resulting in poor resolution (black regions in Fig. 2(a)), including plentiful shear bands

(marked by white arrows). The color variations in each individual grain interior indicate the large changes in interior misorientation (Fig. 2(a)). Low-angle GBs (LAGBs, 2° – 15°) and high-angle GBs (HAGBs, $> 15^\circ$) are marked by yellow and black lines in Fig. 2(b), respectively. The LAGBs spread all over the CR90 sample and have a volume fraction of $\sim 85\%$. There is no 60° TB from the inset in Fig. 2(b), indicating that deformation twinning did not occur during cold-rolling. It was further verified by TEM observation from the view of the RD-ND plane that the CR90 sample is composed of nano-lamellar sub-grains with an average thickness of 72 nm and high-density dislocations (Fig. 2(c)). The corresponding selected area electron diffraction (SAED) pattern shows no twins in the CR90 sample. High-density dislocations existing in the nano lamellae are further revealed by high-resolution TEM image (Fig. 3(a)) and the corresponding inverse fast Fourier transform (IFFT) pattern (Fig. 3(b)). Moreover, some stacking faults (SFs) are observed along LAGBs in the nano lamellae, and two SFs on two conjugated slip planes interact with each other (marked by green arrows in Fig. 3(c)). The IFFT pattern shows the LAGB in Fig. 3(c) is 6.1° (Fig. 3(d)), which is formed by dislocations (marked by white “ \perp ”). From the RD-TD plane (Fig. 2(d)), high-density dislocation walls and cells exist. Therefore, the CR90 sample is a nano-lamella structure, filled with a mass of deformed structures containing dislocation entanglements, walls, cells, SFs, and LAGBs.

3.1.3. Microstructures of as-annealed samples

The microstructures of as-annealed $\text{Ni}_2\text{CoFeV}_{0.5}$ MEAs with the varied HL structures are shown in Fig. 4(a–d). These HL samples are all partially recrystallized and composed of millimeter-sized elongated grains along the rolling direction and a large amount of RGs. Interestingly, most RGs agglomerated into the long lamellae along the rolling direction in all HL samples. Moreover, some RGs are distributed in shear bands with high strain energy, as marked by white arrows in Fig. 4(a–c). As shown in Fig. 4(e), the grain size distributions disregarding TBs show the RGs in all HL samples have similar size distribution trends and a similar average size of about $4\ \mu\text{m}$ (Table 2). The corresponding distributions of the GB misorientation angle are shown in Fig. 4(f). The peak at 60° corresponds to $\Sigma 3$ coincident-site lattice TBs, as marked by the black arrow. The HL-620 $^\circ\text{C}$ -1 h sample has the highest volume fraction of HAGBs with $\sim 66\%$ and the other three HL samples have the approximate HAGB fraction, as listed in Table 2. High-density LAGBs still spread in the elongated deformed grains and high-density TBs were produced in the RGs by annealing. The volume fraction of TBs is 5.8% of HL-590 $^\circ\text{C}$ -1 h, 9.3% of HL-600 $^\circ\text{C}$ -3 h, 10.7% of HL-620 $^\circ\text{C}$ -30 min, and 25.2% of HL-620 $^\circ\text{C}$ -1 h, respectively. Considering that TBs are a kind of HAGBs with specific angles and exhibit superior improvement of strength and ductility synergy compared with HAGBs [39], the volume ratio of TBs and HAGBs was calculated and designated as T/H. The HL-60 $^\circ\text{C}$ -3 h and HL-620 $^\circ\text{C}$ -30 min samples have the approximate volume fractions of T/H (Table 2), indicating the densities of annealing TBs have similar levels. With the increase in annealing temperature, the volume fractions of T/H increased from 17.8% of the HL-590 $^\circ\text{C}$ -1 h sample to 38.1% of the HL-620 $^\circ\text{C}$ -1 h sample, indicating the increased density of annealing TBs.

Due to the limited resolution of the EBSD technique, TEM observation focusing on the HL-590 $^\circ\text{C}$ -1 h and HL-600 $^\circ\text{C}$ -3 h samples were further performed in an attempt to supplement EBSD information. In the HL-590 $^\circ\text{C}$ -1 h sample, it can be found that some submicron-grains with nano-twins recrystallized in the nano-lamellar grains after annealing (Fig. 5(a)). The typical double-oriented twin relationship is verified by the SAED pattern in Fig. 5(b). Moreover, high-density annealing twins including plenty of nano-twins exist in the recrystallized micro-grains (Fig. 5(c)).

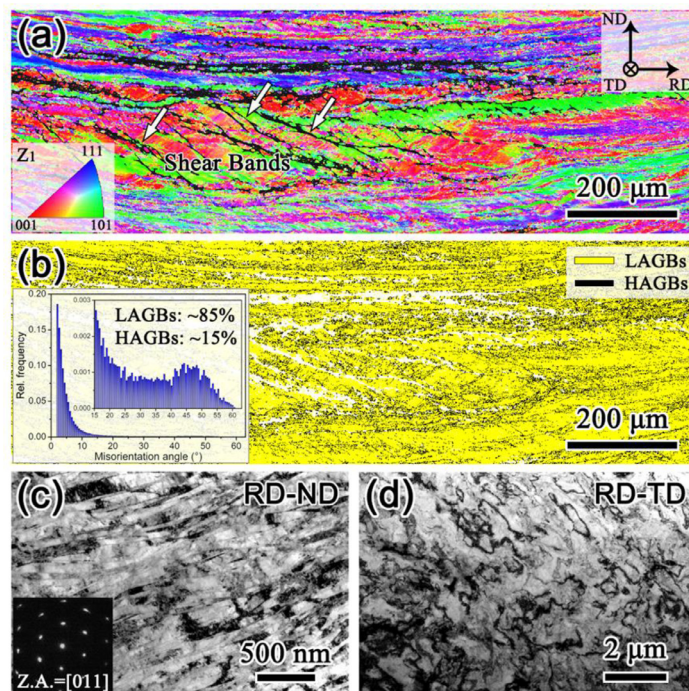


Fig. 2. The microstructures of the cold-rolled $\text{Ni}_2\text{CoFeV}_{0.5}$ MEA. (a) EBSD crystal orientation map with IPF color code of $Z_1 // \text{TD}$. RD: rolling direction; TD: transverse direction; ND: normal direction. (b) GB map with low- and high-angle GBs (LAGBs: $2^\circ\text{--}15^\circ$, HAGBs: $> 15^\circ$) marked by yellow and black lines, respectively. The inset in (b) is the distribution of the GB misorientation angle. Bright-field TEM images from (c) RD-ND and (d) RD-TD plane. The inset in (c) is the corresponding selected area electron diffraction (SAED) pattern with the zone axis of $[011]$.

Table 2

Lists of the volume fraction of HAGBs (F_{HAGBs}), TBs (F_{TBs}), and T/H ($F_{\text{T/H}}$), recrystallization fraction (F_c), average grain size (\bar{d}) and the density of GNDs (ρ) of the HL $\text{Ni}_2\text{CoFeV}_{0.5}$ MEAs from EBSD data.

Samples	F_{HAGBs} (%)	F_{TBs} (%)	$F_{\text{T/H}}$ (%)	F_c (%)	\bar{d} (μm)	ρ ($\times 10^{14} \text{ m}^{-2}$)
HL-590 °C-1 h	32.5	5.8	17.8	23.3	3.7	2.7
HL-600 °C-3 h	36.6	9.3	25.4	39.2	4.3	2.3
HL-620 °C-30 min	37.5	10.7	28.5	45.6	4.0	2.2
HL-620 °C-1 h	66.2	25.2	38.1	76.4	4.3	1.2

As shown in Fig. 6(a), a typical HL structure consisting of recrystallized lamellae (green dashed areas) and non-recrystallized lamellae exists in the HL-600 °C-3 h sample. Moreover, some non-recrystallized grains (NRGs) are distributed in the recrystallized lamellae, surrounded by blue lines in Fig. 6(a). In the RGs, there are high-density annealing twins with an average lamella thickness of 145 nm, as marked by white arrows. The enlarged view of a recrystallized grain shows double-oriented twins (T3, T4) including nano-twins and low-density scattered dislocations (Fig. 6(b)). The typical double-oriented twin relationship is verified by the SAED pattern in Fig. 6(c). The magnified view in Fig. 6(d) shows non-recrystallized zone in the HL-600 °C-3 h sample is composed of nano-lamellar sub-grains with an average thickness of 94 nm, indicating slight growth of nano-lamellar sub-grains after annealing for a long time. Notably, the stable single-phase fcc structure was maintained and no nanoparticle was produced in this severely deformed $\text{Ni}_2\text{CoFeV}_{0.5}$ MEA after annealing at 600 °C for 3 h, as verified by the TEM results, in accord with the XRD result in Fig. 1(d).

The local misorientation maps of HL-590 °C-1 h, HL-600 °C-3 h, HL-620 °C-30 min, and HL-620 °C-1 h $\text{Ni}_2\text{CoFeV}_{0.5}$ MEAs are shown in Fig. 7(a–d). The rainbow color bar from blue to red represents low to high local misorientation, indicating low- to high-density geometrically necessary dislocations (GNDs). The recrystallized areas in all HL MEAs have lower GNDs densities and the non-recrystallized areas have higher stored strain energy. The uneven distribution of strain pre-existed in all HL MEAs. The HL-600

°C-3 h sample shows more green and the other three samples are reddish in the non-recrystallized areas, indicating the lower GNDs densities in the remaining deformed grains of the HL-600 °C-3 h sample. The quantitative Kernel average misorientation (KAM) distributions are shown in Fig. 7(e). Intuitively, the KAM values of all HL samples exhibit a bimodal distribution with the peaks of RGs and NRGs. Comparatively speaking, the peak of NRGs (marked by green arrow) in the HL-600 °C-3 h sample shifts to the left, exhibiting the lowest GNDs densities of NRGs compared to the other three HL samples. Grains with KAM values smaller than 1° were considered as RGs and the recrystallization fraction was calculated, based on the pixel ratio in EBSD data. The volume fractions of RGs in HL-590 °C-1 h, HL-600 °C-3 h, HL-620 °C-30 min, and HL-620 °C-1 h samples are 23.3%, 39.2%, 45.6%, and 76.4%, respectively, as listed in Table 2. The average KAM values of these HL samples are 1.95° , 1.65° , 1.62° , and 0.85° , respectively. The GNDs density has a linear relation with the average KAM value and can be calculated by the formula from the strain gradient theory by Gao et al. [40] and Kubin et al. [41]:

$$\rho = \frac{\theta^{\text{KAM}}}{ub} \quad (1)$$

where ρ is the density of GNDs; u is the step size, which is 500 nm, used in EBSD acquisition; b is the Burgers vector (0.252 nm in use, $b = \sqrt{2}/2a$, $a = 0.357$ nm calculated from XRD results); θ^{KAM} is the averaged KAM value. The calculated GNDs densities

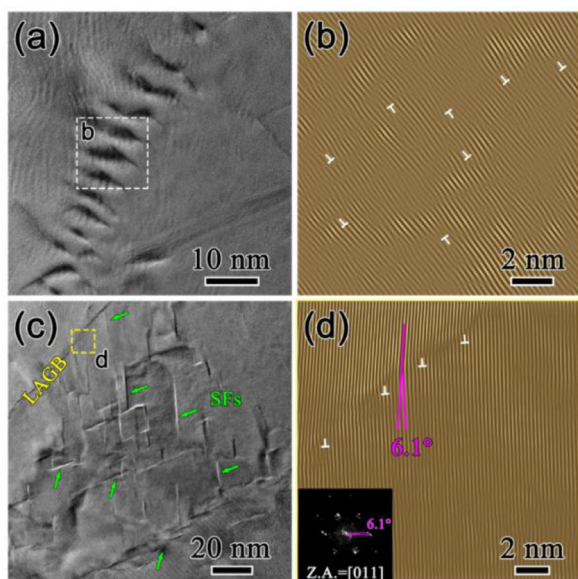


Fig. 3. (a, c) High-resolution TEM images of nano lamellae in the cold-rolled $\text{Ni}_2\text{CoFeV}_{0.5}$ MEA. The stacking faults (SFs) are marked by green arrows. (b, d) The inverse fast Fourier transform (IFFT) patterns obtained from $\{11\bar{1}\}$ reflection, deduced from the white square in (a) and yellow square in (c), respectively. The dislocations are marked by white “ \perp ”.

are $2.7 \times 10^{14} \text{ m}^{-2}$ for HL-590 °C-1 h, $2.3 \times 10^{14} \text{ m}^{-2}$ for HL-600 °C-3 h, $2.2 \times 10^{14} \text{ m}^{-2}$ for HL-620 °C-30 min and $1.2 \times 10^{14} \text{ m}^{-2}$ for HL-620 °C-1 h samples, as listed in Table 2.

Fig. 8(a–d) shows the crystal orientation maps of $\text{Ni}_2\text{CoFeV}_{0.5}$ MEAs annealed at 650 to 900 °C for 1 h. The corresponding distributions of grain size and GB misorientation angle are shown in Fig. 8(e, f). There are a few residual non-recrystallized zones after annealing at 650 °C for 1 h (marked by black lines in Fig. 8(a)), which have high-density dislocations, further confirmed by Fig. 9(a). With the annealing temperature increased to 700 °C, the sample consists of fully-recrystallized grains with an average grain size of 5.5 μm . With further increasing the annealing temperature from 800 to 900 °C, the average grain sizes increase from

9.5 to 14.8 μm . All the fully-recrystallized samples consist of randomly oriented equiaxed grains. After complete recrystallization, the volume fraction of LAGBs drastically reduced to less than 10% and the counterpart of TBs increased to more than 40%. A few scattered LAGBs with higher strain energy (green lines) can be found in the RGs and the corresponding volume fraction increases with the grain growth, as marked by white arrows in Fig. 9(b–d). The average KAM values decrease from 0.36° to 0.24° with the increased annealing temperature from 650 to 900 °C, as shown in Fig. 9(e), indicating a continuous decrease in dislocation density. The densities of GNDs are 5×10^{13} , 4.2×10^{13} , 3.6×10^{13} , and $3.3 \times 10^{13} \text{ m}^{-2}$ after isochronal annealing at 650, 700, 800, and 900 °C, respectively, calculated by the Eq. (1).

3.2. Tensile properties

The representative engineering stress-strain curves of $\text{Ni}_2\text{CoFeV}_{0.5}$ MEAs after thermo-mechanical treatments with different conditions are compared in Fig. 10(a). First, the CR90 sample composed of nano-lamellar grains has a high YS of 1071 MPa and UTS of 1138 MPa but a poor fracture elongation of 8.4%. Furthermore, there is almost no uniform elongation (2.3%) and necking occurs instantaneously after yielding, resulting from the plummeting strain hardening rate (Fig. 10(b)). Interestingly, after annealing at 590 °C for 1 h, the YS and UTS increase to 1120 and 1223 MPa, respectively. Meanwhile, the uniform elongation and fracture elongation of the HL-590 °C-1 h sample increase to 6.1% and 12.3%, respectively. Simultaneous enhancement of strength and ductility occurred in the HL-590 °C-1 h sample. After long-time annealing, the HL-600 °C-3 h sample exhibits a high YS of 981 MPa and a good uniform elongation of 10.2%. In contrast, the HL-620 °C-30 min sample has a lower YS of 860 MPa and a slightly improved uniform elongation of 12.5%. In reality, although the HL-620 °C-1 h sample has a relatively low YS of 783 MPa, the UTS of 982 MPa is comparable to the counterpart of the HL-620 °C-30 min sample (1014 MPa) and the uniform elongation rapidly increased to 17.9%, benefiting from its high strain hardening capacity (Fig. 10(b)). Further increasing the isochronal annealing temperature from 650 to 900 °C, the strength decreases and the ductility increases step by step, as listed in Table 3. Moreover, the drop of strain hardening rates gradually slows and a plateau

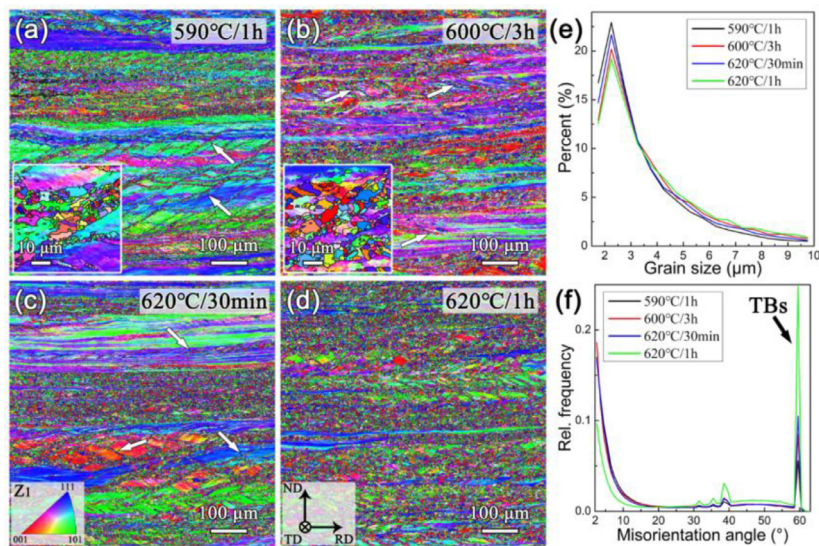


Fig. 4. EBSD crystal orientation maps of the as-annealed $\text{Ni}_2\text{CoFeV}_{0.5}$ MEAs with the varied HL structures: (a) HL-590 °C-1 h; (b) HL-600 °C-3 h; (c) HL-620 °C-30 min and (d) HL-620 °C-1 h. The insets in (a, b) are the local enlarged details. IPF color code of Z_1 is parallel to TD. The corresponding distributions of (e) grain size and (f) GB misorientation angle. TBs: twin boundaries.

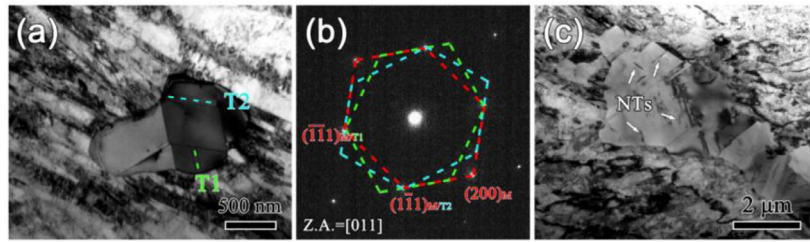


Fig. 5. TEM images of HL-590 °C-1 h $\text{Ni}_2\text{CoFeV}_{0.5}$ MEA from RD-ND plane. (a) A recrystallized submicron-grain embedded in nano lamellae. (b) The SAED pattern of the recrystallized grain in (a), showing double-oriented twins, T1 and T2. (c) High-density annealing nano-twins (NTs) in the recrystallized micro-grains, pointed by white arrows.

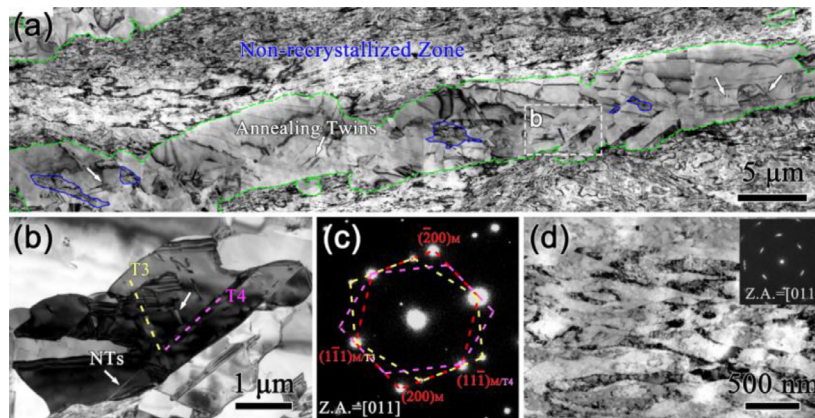


Fig. 6. (a) A low magnification TEM image of HL-600 °C-3 h $\text{Ni}_2\text{CoFeV}_{0.5}$ MEA from RD-ND plane. Green dashed areas in (a) show the recrystallized lamellae and blue areas are the remaining deformed grains. (b) The enlarged view of the square area in (a). NTs: nano-twins. (c) The SAED pattern of the recrystallized grain in (b). (d) The nano lamellae in the non-recrystallized zone and the corresponding SAED pattern.

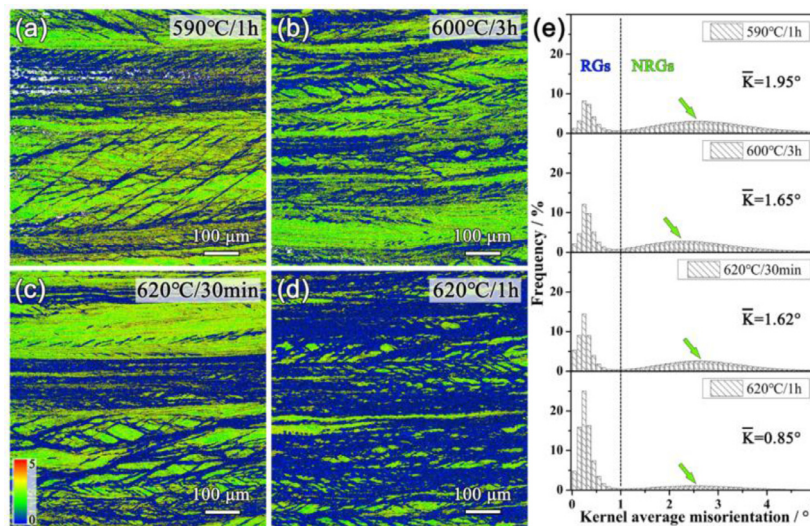


Fig. 7. The local misorientation maps of (a) HL-590 °C-1 h; (b) HL-600 °C-3 h; (c) HL-620 °C-30 min, and (d) HL-620 °C-1 h $\text{Ni}_2\text{CoFeV}_{0.5}$ MEAs. The inset in (c) is the rainbow color bar (blue to red represents low to high misorientation). (e) The corresponding KAM value distributions. \bar{K} : average KAM value. RGs ($K < 1^\circ$): recrystallized grains; NRGs ($K > 1^\circ$): non-recrystallized grains. The peak KAM values of the non-recrystallized zone are pointed by green arrows in (e).

appears in the curve after annealing at 900 °C for 1 h, as shown in Fig. 10(b).

3.3. Microstructures after tensile deformation

TEM analysis in the recrystallized zone of HL-600 °C-3 h $\text{Ni}_2\text{CoFeV}_{0.5}$ MEA at necking was performed to reveal the deformation mechanisms. The dark-field TEM image (Fig. 11(a)) shows there are high-density dislocations and a small number of twins in the micron-sized grain. The typical coherent twin relationship is confirmed by the inserted SAED pattern. Notably, these twins are

stepped or isolated, which are annealing twins, different from the morphology of deformation twins [42]. In our previous study [43], the lathy deformation twins are parallel with each other and emit from HAGBs. Therefore, deformation twinning did not occur in the $\text{Ni}_2\text{CoFeV}_{0.5}$ MEA under tension at ambient temperature. Fig. 11(b) shows a micro-sized grain divided by twin networks accumulated a large number of dislocations. The enlarged details indicate that there are various dislocation configurations, including parallel dislocation arrays, pile-ups, and entanglements, as shown in Fig. 11(c, d). High-density dislocations piled up at the annealing TBs and also accumulated inside the annealing twins. Moreover, the dif-

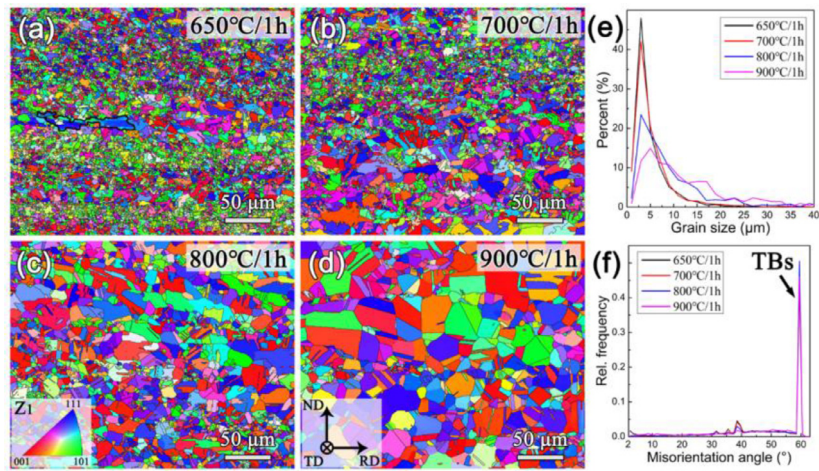


Fig. 8. EBSD crystal orientation maps of $\text{Ni}_2\text{CoFeV}_{0.5}$ MEAs annealed at (a) 650 °C; (b) 700 °C; (c) 800 °C, and (d) 900 °C for 1 h. IPF color code of Z_1 is parallel to TD. The corresponding distributions of (e) grain size and (f) GB misorientation angle.

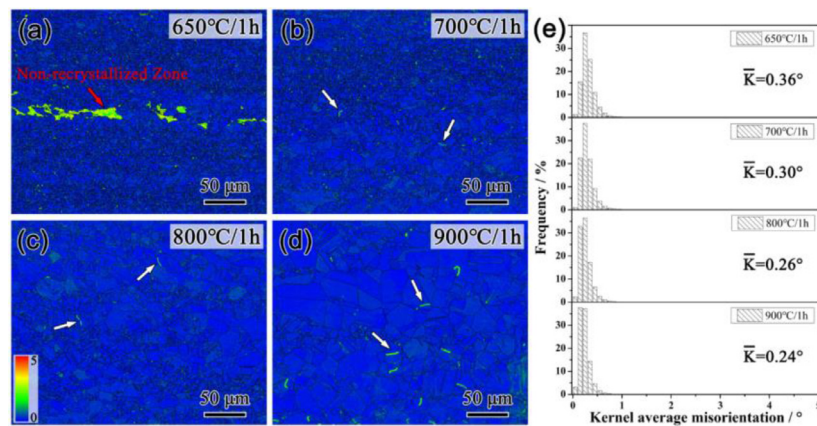


Fig. 9. The local misorientation maps of $\text{Ni}_2\text{CoFeV}_{0.5}$ MEAs annealed at (a) 650 °C; (b) 700 °C; (c) 800 °C, and (d) 900 °C for 1 h. The sub-grain boundaries are pointed by white arrows. (e) The corresponding distributions of KAM value.

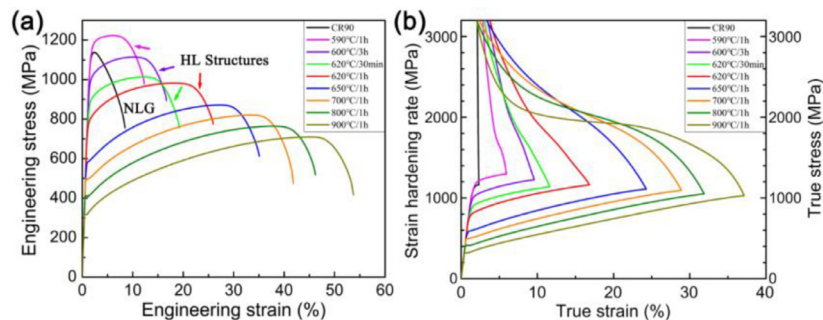


Fig. 10. Tensile properties of $\text{Ni}_2\text{CoFeV}_{0.5}$ MEAs after thermo-mechanical treatments with different conditions. (a) Engineering stress-strain curves. (b) True stress and strain hardening rate versus true strain. NLG: nano-lamellar grain.

fusely distributed nano-twins in the HL-600 °C-3 h sample can also act as an efficient barrier to impede the movement of dislocations (Fig. 12(a)). It can be found that abundant fine SFs transmitted from the TB, indicating SFs mediated the plastic deformation and avoided the stress concentration at TBs (Fig. 12(b)).

3.4. HDI stress measurement

To reveal the contribution of HDI stresses on the tensile properties of $\text{Ni}_2\text{CoFeV}_{0.5}$ MEAs with HL structures, the LUR tensile tests were performed to estimate the effect of HDI strengthening and hardening. Fig. 13 shows the typical true stress-strain curves

and the evolution of HDI stresses with the increased strain of HL-590 °C-1 h, HL-600 °C-3 h, HL-620 °C-30 min, and HL-620 °C-1 h $\text{Ni}_2\text{CoFeV}_{0.5}$ MEAs. The hysteresis loops indicate the existence of inhomogeneous deformation in all HL samples. The HDI stresses (σ_{HDI}) at different strains were calculated by the following equation [44,45]:

$$\sigma_{\text{HDI}} = \frac{\sigma_r + \sigma_u}{2} \quad (2)$$

where the σ_r and σ_u are the reloading and unloading yield stresses, respectively, measured from each hysteresis loop. For all HL samples, the measured HDI stresses almost monotonically in-

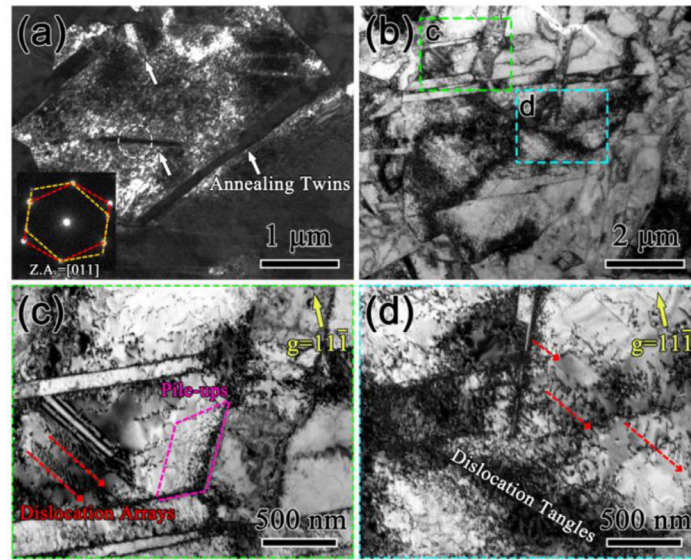


Fig. 11. Typical microstructures in the recrystallized zone of HL-600 °C-3 h $\text{Ni}_2\text{CoFeV}_{0.5}$ MEA at necking. (a) Dark-field TEM image and the SAED pattern of the circled area, showing reserved annealing twins and dislocation structures. (b) Bright-field TEM image of micro-sized grain divided by twin networks. (c, d) Magnified regions in (b) showing various dislocation configurations, including parallel dislocation arrays, pile-ups, and dislocation tangles.

Table 3

Lists of YS, ultimate tensile strength (UTS), uniform elongation ε_{ue} , and elongation to failure ε_{ef} of $\text{Ni}_2\text{CoFeV}_{0.5}$ MEAs after thermo-mechanical treatments with different conditions.

Samples	YS (MPa)	UTS (MPa)	ε_{ue} (%)	ε_{ef} (%)
CR90	1071	1138	2.3	8.4
590 °C/1 h	1120	1223	6.1	12.3
600 °C/3 h	981	1114	10.2	16.7
620 °C/30 min	860	1014	12.5	19.3
620 °C/1 h	783	982	17.9	25.9
650 °C/1 h	583	872	27.4	35.0
700 °C/1 h	492	821	33.2	41.8
800 °C/1 h	411	764	37.6	46.2
900 °C/1 h	317	711	44.9	53.7

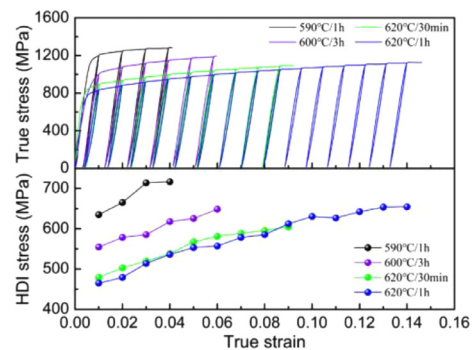


Fig. 13. The cyclic load-unload-reload curves and the evolution of hetero-deformation-induced stresses with an applied strain of HL $\text{Ni}_2\text{CoFeV}_{0.5}$ MEAs.

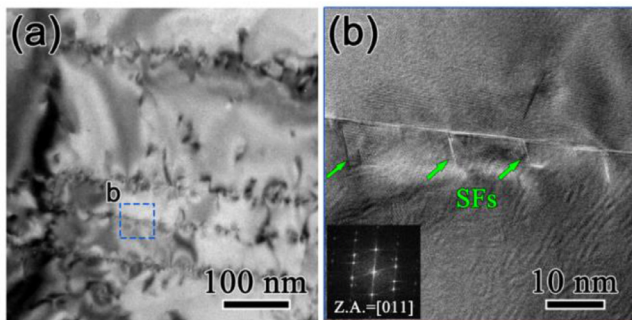


Fig. 12. (a) Bright-field TEM image of nano-twins and (b) high-resolution TEM image magnified from TB (blue square in (a)) in the recrystallized zone of HL-600 °C-3 h $\text{Ni}_2\text{CoFeV}_{0.5}$ MEA at necking. High-density dislocations entangled at TBs, and SFs (marked by green arrows) transmitted from TB.

crease with the continuous plastic deformation due to the accumulation of GNDs at the HAGBs, TBs, and the interface of soft/hard domains. The HL-620 °C-30 min and HL-620 °C-1 h samples have the approximative HDI stresses at the same strain levels, indicating little difference in the contribution of HDI strengthening and hardening. Nonetheless, the HDI stresses in HL-590 °C-1 h and HL-600 °C-3 h samples are significantly elevated, and increased from 634.9 to 716.5 MPa and 554.6 to 617.7 MPa within the strain range from 0.01 to 0.04, respectively.

4. Discussion

4.1. Microstructure-property relationship of HL structure

The HL $\text{Ni}_2\text{CoFeV}_{0.5}$ MEAs were constructed by partial recrystallization annealing on the cold-rolled sample. Firstly, the CR90 sample underwent severe plastic deformation and plenty of deformation structures were produced inside. High-density LAGBs, dislocations, and SFs contributed to the high YS of the CR90 sample over 1 GPa. There is no surprise that the CR90 sample rapidly became plastic instability and necking occurred after yielding, due to its nearly null strain hardening capability and poor dislocation storage capability. After intermediate temperature annealing, the recrystallized lamellae with micro-sized RGs ($\sim 4 \mu\text{m}$) formed. Typical HL structures with soft domains (micro-grain lamellae) and hard domains (nano-/ultrafine-grain lamellae) formed in all HL-590 °C-1 h, HL-600 °C-3 h, HL-620 °C-30 min, and HL-620 °C-1 h samples (Fig. 4). Nevertheless, these HL samples exhibited varied tensile behaviors (Fig. 10), resulting from their different microstructural parameters.

For the HL-590 °C-1 h sample, simultaneously improved strength and ductility occurred after annealing, compared with the CR90 sample. The YS and UTS increased by 5% and 7%, and the uniform elongation and total elongation increased by 165%

and 46%, respectively. Normally, softening occurs in most metallic materials along with the recrystallization process [46–49]. However, annealing-induced strengthening occurred in the HL-590 °C-1 h sample, which had ~23 vol% RGs. This phenomenon may be mainly attributed to the following three reasons. First, high-density annealing TBs exist in the RGs, which can increase the critical stress for dislocation slip, thereby increasing the strength of recrystallized zones. Likewise, Lu et al. and Duan et al. [50] fabricated nano-twinned Cu and Ni, respectively, both of which had ultra-high strength compared with CG counterparts. Second, the annihilation of mobile dislocations inside the NRGs results in higher applied stress for the activation of dislocations. This can be verified by the slightly decreasing dislocation density from $3.6 \times 10^{14} \text{ m}^{-2}$ of the CR90 sample to $2.5 \times 10^{14} \text{ m}^{-2}$ of the non-recrystallized zones in the HL-590 °C-1 h sample. Liang et al. [51] also found that annealing-induced hardening occurred below 600 °C in a nanocrystalline fcc $\text{FeNi}_2\text{CoMo}_{0.2}\text{V}_{0.5}$ HEA without precipitation effect, resulting from the annihilation of mobile dislocations and sustained deformation twin barriers. Third, extra HDI strengthening produced by the HL structure enhances the global YS. At the initial stage of tensile deformation, although the recrystallized zones (soft domains) had plastically deformed, the non-recrystallized zones (hard domains) were still elastically deformed. The dominating hard domains led to global elastic deformation. Moreover, the dispersed RGs lamellae in shear bands were restricted by the non-recrystallized matrix during deformation. Extra HDI stresses formed at the interfaces of soft/hard lamellae, contributing to the higher YS of the HL-590 °C-1 h sample. For most MEAs/HEAs, the extensive mechanism of annealing-induced strengthening is the formation of a precipitated phase after intermediate temperature annealing [52–54]. However, in these $\text{Ni}_2\text{CoFeV}_{0.5}$ MEAs, no second phase was detected by XRD (Fig. 1(d)) and TEM (Figs. 5 and 6) results after annealing at 590 °C for 1 h and 600 °C for 3 h and a stable fcc single-phase was retained. Moreover, the HL-590 °C-1 h sample had a decent ductility of ~12%, distinctly different from the precipitate-strengthened MEAs/HEAs, which have poor ductility [53,54]. After partial recrystallization via annealing, the HL-590 °C-1 h sample consists of ~23 vol% RGs, which can accumulate plenty of dislocations during tensile deformation, provide strain hardening, and regain tensile ductility.

With further recrystallization, the strength gradually decreased and the ductility was gradually restored. The HL-600 °C-3 h and HL-620 °C-30 min samples had an approximate fraction of recrystallization, which are 39.2% and 45.6%, respectively. Nonetheless, the HL-620 °C-30 min sample had similar ductility but lower strength compared with the HL-600 °C-3 h sample, as listed in Table 3. Although the above-mentioned two samples had similar volume fraction ratios of soft and hard lamellae, the spatial distribution of soft lamellae, i.e. interface spacing, are visibly different (Fig. 4(b, c)). Soft lamellae in the HL-600 °C-3 h sample are more diffusely distributed and the interface spacing of soft and hard lamellae is smaller, which is conducive to producing more HDI stresses, as verified in Fig. 13. Huang et al. [55] have reported that the optimal interface spacing of 15 μm achieved the maximized strength and ductility synergy in the lamella structure material. While the interface spacing is larger than 15 μm , the strength and ductility synchronously enhanced with the decreasing interface spacing [55,56]. In addition, the difference in flow stress between soft/hard domains also can influence the role of HDI hardening. If hard domains cannot plastically deform or are hard to deform, stress concentration may occur at the interface of soft/hard domains, leading to crack initiation at the interface. For the HL-600 °C-3 h sample, the hard lamellae had lower dislocation densities (Fig. 7(e)), benefiting from long-time annealing. Comparatively speaking, the HL-620 °C-30 min sample had higher dislocation densities in the hard lamellae, which may lead to excessive

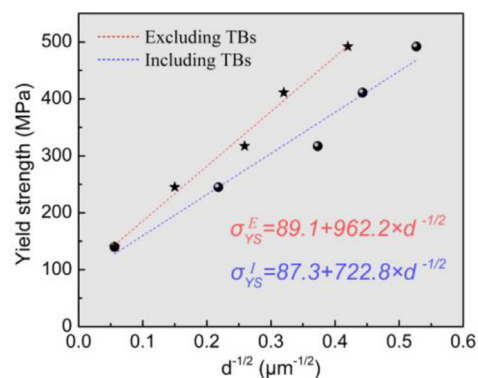


Fig. 14. Hall-Petch relationship of $\text{Ni}_2\text{CoFeV}_{0.5}$ MEAs: yield strength as a function of grain size at the micro-sized level. Blue and red dashed lines are the fitted curves including and excluding annealing TBs, respectively.

stress concentration at the interface of soft/hard domains, thereby causing premature failure fracture at the interface. Furthermore, after annealing at 620 °C for 1 h, the volume fraction of recrystallization increased to 76.4%. The HL-620 °C-1 h sample had a high YS of ~780 MPa and good ductility of ~26%. The ~25 vol% hard lamellae embedded in the RGs matrix can effectively improve the strength. Therefore, for metallic materials with HL structure, in addition to the volume fraction ratio of soft and hard lamellae, the strength difference and the interface spacing or interface densities can also influence the role of synergistic strengthening of soft and hard lamellae.

4.2. Hall-Petch relationship

For polycrystalline metallic materials, the YS (σ_{YS}) often has a good inverse relation with the average grain size (d), that is the YS increases with the grain size decreases, which can be described by the classical Hall-Petch relation [57,58].

$$\sigma_{\text{YS}} = \sigma_0 + kd^{-1/2} \quad (3)$$

where σ_0 is the lattice friction stress, and k is the Hall-Petch coefficient for GB strengthening. According to the experimental results of the YS obtained by different thermo-mechanical treatments, the Hall-Petch relationship of $\text{Ni}_2\text{CoFeV}_{0.5}$ MEA including and excluding annealing TBs were plotted in Fig. 14, respectively. It can be found that the lattice friction stress of $\text{Ni}_2\text{CoFeV}_{0.5}$ MEA is a constant of ~90 MPa whether TBs are included or not. However, the Hall-Petch coefficients are quite different, 722.8 $\text{MPa } \mu\text{m}^{1/2}$ when including TBs and 962.2 $\text{MPa } \mu\text{m}^{1/2}$ when excluding TBs, respectively. Similar results were reported in CrCoNi MEA, which also has a large number of annealing TBs in the RGs [59]. The authors believed that crystallite size (which counts both annealing TBs and GBs) is a more relevant length scale to characterize Hall-Petch strengthening because TBs do act as obstacles to dislocation motion at the early stage of plastic deformation [59]. Therefore, considering the TB is a kind of GB with a specific angle, which has a function of strengthening, the TBs were counted to calculate the average grain size. After linear fitting (blue dashed line), σ_0 and k of $\text{Ni}_2\text{CoFeV}_{0.5}$ MEA were calculated to be 87.3 MPa and 722.8 $\text{MPa } \mu\text{m}^{1/2}$, respectively. Chung et al. [60] found that σ_0 increased from 216 to 383 MPa with increasing V content from CrCoNi to VCoNi. For our $\text{Ni}_2\text{CoFeV}_{0.5}$ MEA, the lattice friction stress also increases from ~60 MPa of CoFeNi MEA [61] to ~90 MPa with the addition of V. It means that adding V in MEAs/HEAs can effectively hinder dislocation slip, thereby strengthening and toughening materials. Yin et al. [62] also reported that V is an optimal element for strengthening in both fcc and bcc HEAs because of its large misfit volume. Moreover, the large Hall-Petch coefficient of $\text{Ni}_2\text{CoFeV}_{0.5}$

MEA indicates the prominent effect of GB strengthening, which is nearly twice as much as CoFeNi MEA ($366 \text{ MPa } \mu\text{m}^{1/2}$) [61].

5. Conclusions

In this work, we tuned the microstructures of single-phase fcc $\text{Ni}_2\text{CoFeV}_{0.5}$ MEAs by means of cold-rolling followed by annealing and then tested their tensile properties. Systematic investigations were performed by EBSD and TEM to investigate the microstructural evolution after thermo-mechanical treatments and reveal the deformation mechanisms under tension. The main conclusions are as follows:

- (1) The $\text{Ni}_2\text{CoFeV}_{0.5}$ MEA had a high YS of 1071 MPa but a poor ductility of 8.4% after cold-rolling, attributed to numerous deformed structures containing high-density dislocation entanglements, walls, cells, SFs, and LAGBs. After partial annealing, the typical HL structure consisting of recrystallized micro-grain lamellae and non-recrystallized nano-/ultrafine-grain lamellae were obtained.
- (2) Simultaneous enhancement of strength and ductility occurred in the HL-590 °C-1 h sample, compared with the CR90 sample. Extraordinarily, with ~23 vol% RGs, the YS and UTS of the HL-590 °C-1 h sample increased by 5% and 7%. Annealing-induced strengthening is attributed to high-density annealing TBs in the RGs, the annihilation of mobile dislocations inside the NRGs, and extra HDI strengthening produced by the HL structure.
- (3) The HL-620 °C-30 min sample had approximate ductility but lower strength compared with the HL-600 °C-3 h sample. Both samples have similar volume fraction ratio of soft and hard lamellae, but the spatial distribution of soft lamellae are visibly different. That is because smaller interface spacing and higher interface density of soft/hard lamellae contributed to more significant HDI strengthening and hardening. Moreover, the HL-620 °C-30 min sample had higher dislocation densities in the hard lamellae, which will lead to excessive stress concentration at the interface of soft/hard lamellae.
- (4) The Hall-Petch relationship of $\text{Ni}_2\text{CoFeV}_{0.5}$ MEA can be reasonably described by counting both TBs and GBs. The lattice friction stress (σ_0) and the Hall-Petch coefficient (k) are 87.3 MPa and $722.8 \text{ MPa } \mu\text{m}^{1/2}$, respectively.

CRedit authorship contribution statement

Lei Gu: Conceptualization, Data curation, Visualization, Investigation, Methodology, Writing – original draft. **Rui Hou:** Visualization, Investigation, Methodology. **Yi Liu:** Investigation, Methodology. **Guang Chen:** Supervision, Funding acquisition. **Jihua Liu:** Investigation. **Gong Zheng:** Funding acquisition. **Ruisheng Zhang:** Investigation. **Yonghao Zhao:** Validation, Supervision, Funding acquisition, Writing – review & editing.

Acknowledgements

This work was financially supported by the National Key R&D Program of China (Grant No. 2021YFA1200203), National Natural Science Foundation of China (Grant Nos. 51971112, 51225102, 92163215, 52174364, 52101143, 51731006, and 12202201), Natural Science Foundation of Jiangsu Province Major Project (Grant No. BK20212009) and the Fundamental Research Funds for the Central Universities (Grant Nos. 30922010202, 30922010711, and 30919011405). The authors also want to acknowledge the support of the Jiangsu Key Laboratory of Advanced Micro-Nano Materials and Technology. SEM, TEM, and EBSD experiments are performed at the Center of Analytical Facilities Nanjing University of Science and Technology. L. Gu acknowledges the support of the Large-scale

Instrument and Equipment Open Fund of Nanjing University of Science and Technology.

References

- [1] J.W. Yeh, S.K. Chen, S.J. Lin, J.Y. Gan, T.S. Chin, T.T. Shun, C.H. Tsau, S.Y. Chang, *Adv. Eng. Mater.* 6 (2004) 299–303.
- [2] B. Cantor, I.T.H. Chang, P. Knight, A.J.B. Vincent, *Mater. Sci. Eng. A-Struct. Mater. Prop. Microstruct. Process.* 375–377 (2004) 213–218.
- [3] X.Z. Gao, Y.P. Lu, B. Zhang, N.N. Liang, G.Z. Wu, G. Sha, J.Z. Liu, Y.H. Zhao, *Acta Mater.* 141 (2017) 59–66.
- [4] W. Jiang, S.Y. Yuan, Y. Cao, Y. Zhang, Y.H. Zhao, *Acta Mater.* 213 (2021) 116982.
- [5] Y.P. Lu, X.Z. Gao, L. Jiang, Z.N. Chen, T.M. Wang, J.C. Jie, H.J. Kang, Y.B. Zhang, S. Guo, H.H. Ruan, Y.H. Zhao, Z.Q. Cao, T.J. Li, *Acta Mater.* 124 (2017) 143–150.
- [6] D.B. Miracle, J.D. Miller, O.N. Senkov, C. Woodward, M.D. Uchic, J. Tiley, *Entropy* 16 (2014) 494–525.
- [7] Z.F. Lei, X.J. Liu, Y. Wu, H. Wang, S.H. Jiang, S.D. Wang, X.D. Hui, Y.D. Wu, B. Gault, P. Kontis, D. Raabe, L. Gu, Q.H. Zhang, H.W. Chen, H.T. Wang, J.B. Liu, K. An, Q.S. Zeng, T. Nieh, Z.P. Lu, *Nature* 563 (2018) 546–550.
- [8] B.J. Wang, Q.Q. Wang, N. Lu, X.B. Liang, B.L. Shen, *J. Mater. Sci. Technol.* 123 (2022) 191–200.
- [9] L. Gu, N.N. Liang, Y. Liu, Y.Y. Chen, J.H. Liu, Y.X. Sun, Y.H. Zhao, *Mater. Lett.* 324 (2022) 132676.
- [10] J.J. Wang, Z.D. Kou, S. Fu, S.S. Wu, S.N. Liu, M.Y. Yan, Z.Q. Ren, D. Wang, Z.S. You, S. Lan, H. Hahn, X. Wang, T. Feng, *J. Mater. Sci. Technol.* 115 (2022) 29–39.
- [11] P. Edalati, A. Mohammadi, M. Ketabchi, K. Edalati, *J. Alloy. Compd.* 884 (2021) 161101.
- [12] Y.P. Lu, H.F. Huang, X.Z. Gao, C.L. Ren, J. Gao, H.Z. Zhang, S.J. Zheng, Q.Q. Jin, Y.H. Zhao, C.Y. Lu, T.M. Wang, T.J. Li, *J. Mater. Sci. Technol.* 35 (2019) 369–373.
- [13] Z.X. Su, T. Shi, J.X. Yang, H.H. Shen, Z.M. Li, S. Wang, G. Ran, C.Y. Lu, *Acta Mater.* 233 (2022) 117955.
- [14] N.T. Nguyen, P. Asghari-Rad, P. Sathiyamoorthi, A. Zargarani, C.S. Lee, H.S. Kim, *Nat. Commun.* 11 (2020) 2736.
- [15] B. Gludovatz, A. Hohenwarter, D. Catoor, E.H. Chang, E.P. George, R.O. Ritchie, *Science* 345 (2014) 1153–1157.
- [16] W. Jiang, X.Z. Gao, Y. Cao, Y.F. Liu, Q.Z. Mao, L. Gu, Y.H. Zhao, *Mater. Sci. Eng. A-Struct. Mater. Prop. Microstruct. Process.* 837 (2022) 142735.
- [17] Y. Xing, C.J. Li, Y.K. Mu, Y.D. Jia, K.K. Song, J. Tan, G. Wang, Z.Q. Zhang, J.H. Yi, J. Eckert, *J. Mater. Sci. Technol.* 132 (2023) 119–131.
- [18] R.P. Zhang, S.T. Zhao, J. Ding, Y. Chong, T. Jia, C. Ophus, M. Asta, R.O. Ritchie, A.M. Minor, *Nature* 581 (2020) 283–287.
- [19] X.F. Chen, Q. Wang, Z.Y. Cheng, M.L. Zhu, H. Zhou, P. Jiang, L.L. Zhou, Q.Q. Xue, F.P. Yuan, J. Zhu, X.L. Wu, E. Ma, *Nature* 592 (2021) 712–716.
- [20] F. He, S.L. Wei, J.L. Cann, Z.J. Wang, J.C. Wang, C.C. Tasan, *Acta Mater.* 220 (2021) 117314.
- [21] D.X. Wei, L.Q. Wang, Y.J. Zhang, W. Gong, T. Tsuru, I. Lobzenko, J. Jiang, S. Harjo, T. Kawasaki, J.W. Bae, W.J. Lu, Z. Lu, Y. Hayasaka, T. Kiguchi, N.L. Okamoto, T. Ichitsubo, H.S. Kim, T. Furuhashi, E. Ma, H. Kato, *Acta Mater.* 225 (2022) 117571.
- [22] Z.F. He, N. Jia, H.L. Yan, Y.F. Shen, M.W. Zhu, X.J. Guan, X.L. Zhao, S.B. Jin, G. Sha, Y.T. Zhu, C.T. Liu, *Int. J. Plast.* 139 (2021) 102965.
- [23] T. Yang, Y.L. Zhao, Y. Tong, Z.B. Jiao, J. Wei, J.X. Cai, X.D. Han, D. Chen, A. Hu, J.J. Kai, K. Lu, Y. Liu, C.T. Liu, *Science* 362 (2018) 933–937.
- [24] Z. Wu, H. Bei, G.M. Pharr, E.P. George, *Acta Mater.* 81 (2014) 428–441.
- [25] Y. Yang, T.Y. Chen, L.Z. Tan, J.D. Poplawsky, K. An, Y.L. Wang, G.D. Samolyuk, K. Littrell, A.R. Lupini, A. Borisevich, E.P. George, *Nature* 595 (2021) 245–249.
- [26] L.Y. Liu, Y. Zhang, J.H. Han, X.Y. Wang, W.Q. Jiang, C.T. Liu, Z.W. Zhang, P.K. Liaw, *Adv. Sci.* 8 (2021) 2100870.
- [27] R. Fan, L.P. Wang, L.L. Zhao, L. Wang, S.C. Zhao, Y.J. Zhang, B. Cui, *Mater. Sci. Eng. A-Struct. Mater. Prop. Microstruct. Process.* 829 (2022) 142153.
- [28] X.Z. Gao, Y.P. Lu, J.Z. Liu, J. Wang, T.M. Wang, Y.H. Zhao, *Materialia* 8 (2019) 100485.
- [29] Z.M. Li, K.G. Pradeep, Y. Deng, D. Raabe, C.C. Tasan, *Nature* 534 (2016) 227–230.
- [30] P. Sathiyamoorthi, H.S. Kim, *Prog. Mater. Sci.* 123 (2022) 100709.
- [31] Y. Cao, S. Ni, X.Z. Liao, M. Song, Y.T. Zhu, *Mater. Sci. Eng. R-Rep.* 133 (2018) 1–59.
- [32] Q.Z. Mao, Y.F. Liu, Y.H. Zhao, *J. Alloy. Compd.* 896 (2022) 163122.
- [33] Y.H. Zhao, J.F. Bingert, X.Z. Liao, B.Z. Cui, K. Han, A.V. Serhuceeva, A.K. Mukherjee, R.Z. Valiev, T.G. Langdon, Y.T. Zhu, *Adv. Mater.* 18 (2006) 2949–2953.
- [34] W.J. Lu, K. Yan, X. Luo, Y.T. Wang, L. Hou, P.T. Li, B. Huang, Y.Q. Yang, *J. Mater. Sci. Technol.* 98 (2022) 197–204.
- [35] Y.T. Zhu, K. Ameyama, P.M. Anderson, I.J. Beyerlein, H.J. Gao, H.S. Kim, E. Lavrenia, S. Mathaudhu, H. Mughrabi, R.O. Ritchie, N. Tsuji, X.Y. Zhang, X.L. Wu, *Mater. Res. Lett.* 9 (2021) 1–31.
- [36] Q.S. Pan, L.X. Zhang, R. Feng, Q.H. Lu, K. An, A.C. Chuang, J.D. Poplawsky, P.K. Liaw, L. Lu, *Science* 374 (2021) 984–989.
- [37] Y. Yin, Q.Y. Tan, Q. Sun, W.R. Ren, J.Q. Zhang, S.Y. Liu, Y.G. Liu, M. Birmingham, H.W. Chen, M.X. Zhang, *J. Mater. Sci. Technol.* 96 (2022) 113–125.
- [38] W.J. Lu, X. Luo, D. Ning, M. Wang, C. Yang, M.Q. Li, Y.Q. Yang, P.T. Li, B. Huang, *J. Mater. Sci. Technol.* 112 (2022) 195–201.
- [39] L. Lu, X. Chen, X. Huang, K. Lu, *Science* 323 (2009) 607–610.
- [40] H. Gao, Y. Huang, W.D. Nix, J.W. Hutchinson, *J. Mech. Phys. Solids* 47 (1999) 1239–1263.
- [41] L.P. Kubin, A. Mortensen, *Scr. Mater.* 48 (2003) 119–125.
- [42] X.H. An, S.D. Wu, Z.G. Wang, Z.F. Zhang, *Prog. Mater. Sci.* 101 (2019) 1–45.

- [43] L. Gu, N.N. Liang, Y.Y. Chen, Y.H. Zhao, *J. Alloy. Compd.* 906 (2022) 164401.
- [44] M.X. Yang, Y. Pan, F.P. Yuan, Y.T. Zhu, X.L. Wu, *Mater. Res. Lett.* 4 (2016) 145–151.
- [45] Y.F. Liu, Y. Cao, Q.Z. Mao, H. Zhou, Y.H. Zhao, W. Jiang, Y. Liu, J.T. Wang, Z.S. You, Y.T. Zhu, *Acta Mater.* 189 (2020) 129–144.
- [46] Q.Z. Mao, Y.S. Zhang, J.Z. Liu, Y.H. Zhao, *Nano Lett.* 21 (2021) 3191–3197.
- [47] J.H. Li, K.J. Lu, X.J. Zhao, X.K. Ma, F.G. Li, H.B. Pan, J.M. Chen, *J. Mater. Sci. Technol.* 131 (2022) 185–194.
- [48] Y.Z. Wu, K.G. Luo, Y. Zhang, C. Kong, H.L. Yu, *J. Alloy. Compd.* 921 (2022) 166166.
- [49] J.E. Lin, B.L. Yuan, C.Q. Li, Y. Dong, P. Zhang, Z.R. Zhang, *Mater. Lett.* 314 (2022) 131879.
- [50] F.H. Duan, Y. Lin, J. Pan, L. Zhao, Q. Guo, D. Zhang, Y. Li, *Sci. Adv.* 7 (2021) eabg5113.
- [51] N.N. Liang, R.R. Xu, G.Z. Wu, X.Z. Gao, Y.H. Zhao, *Mater. Sci. Eng. A-Struct. Mater. Prop. Microstruct. Process.* 848 (2022) 143399.
- [52] W.H. Liu, Z.P. Lu, J.Y. He, J.H. Luan, Z.J. Wang, B. Liu, Y. Liu, M.W. Chen, C.T. Liu, *Acta Mater.* 116 (2016) 332–342.
- [53] H.T. Jeong, W.J. Kim, *J. Mater. Sci. Technol.* 71 (2021) 228–240.
- [54] X. Bai, W. Fang, R.B. Chang, H.Y. Yu, X. Zhang, F.X. Yin, *Mater. Sci. Eng. A-Struct. Mater. Prop. Microstruct. Process.* 767 (2019) 138403.
- [55] C.X. Huang, Y.F. Wang, X.L. Ma, S. Yin, H.W. Höppel, M. Göken, X.L. Wu, H.J. Gao, Y.T. Zhu, *Mater. Today* 21 (2018) 713–719.
- [56] X.L. Ma, C.X. Huang, J. Moering, M. Ruppert, H.W. Höppel, M. Göken, J. Narayan, Y. Zhu, *Acta Mater.* 116 (2016) 43–52.
- [57] E.O. Hall, *Proc. Phys. Soc. Sec. B* 64 (1951) 747–753.
- [58] N.J. Petch, *J. Iron Steel Inst.* 174 (1953) 25–28.
- [59] M. Schneider, E.P. George, T.J. Manescau, T. Zálezák, J. Hunfeld, A. Dlouhý, G. Eggeler, G. Laplanche, *Int. J. Plast.* 124 (2020) 155–169.
- [60] H. Chung, D.W. Kim, W.J. Cho, H.N. Han, Y. Ikeda, S. Ishibashi, F. Körmann, S.S. Sohn, *J. Mater. Sci. Technol.* 108 (2022) 270–280.
- [61] S. Yoshida, T. Ikeuchi, T. Bhattacharjee, Y. Bai, A. Shibata, N. Tsuji, *Acta Mater.* 171 (2019) 201–215.
- [62] B.L. Yin, F. Maresca, W.A. Curtin, *Acta Mater.* 188 (2020) 486–491.